ADVANCED OPTICAL MATERIALS
www.advopticalmat.de

Inert Gas Element as Active Infrared-Absorption Source and Donor in Silicon for Forbidden-Wavelength Sensing

Nian-Ke Chen, Yu-Chen Gao, Ji-Hong Zhao, Chun-Hao Li, Qi-Dai Chen, Hong-Bo Sun,* Shengbai Zhang,* and Xian-Bin Li**

Intrinsic silicon (Si) is forbidden for infrared (IR) sensing at the communication wavelength like 1.31 or 1.55 µm due to the well-known bandgap limitation. In this work, an unexpected physical picture of using argon (Ar) is identified, which is usually inert to the surrounding chemical environment and used as a protective agent in semiconductor processing, to overcome the IR-sensing-forbidden problem in Si. Here, it is shown by an analysis of a dynamic secondary ion mass spectrometer that such a Si, when exposed to laser pulse in Ar gas, can contain a very high dose of Ar up to 10^{20} cm^{-3} even after 1300 days. First-principles calculations, molecular dynamics, and Hall effect measurements reveal that, due to both steric and dynamic repulsions by Ar orbitals to Si dangling bonds, the Ar-filled-vacancy produces a much wider defect band inside the gap, which is not only responsible for strong infrared absorption, but also causes a significant increase in n-type conductivity, both in line with experiments. The study proves that originally inert elements in fact can act as active impurities in semiconductors for advanced applications, which updates the current knowledge of defect physics.

1. Introduction

Silicon (Si) based optoelectronics is at the heart of the opto-electronic industry owing to its unique ability for Si device integration.[1–9] Among them, photodetectors working at infrared (IR) communication wavelength (λ) of 1.31/1.55 µm are particularly important.[10,11] However, due to the well-known problem of low absorption at $\lambda \geq 1.1$ µm, corresponding to its bandgap, Si is not a candidate for communication applications. Often, another semiconductor like InGaAs or InSb,[12–15] with a suitable bandgap is heterogeneously grown on Si. However, issues with heteroepitaxy such as lattice mismatch can reduce or even degrade the performance.[16] Recently, the integration of 2D materials on Si is also explored for IR photodetection.[17] Another way is to induce IR absorption sources inside Si. For example, gap states can be created by chalcogenide doping with the help of ultrafast laser irradiation to result in black silicon (*b*-Si).[18–23] It has a strong IR absorption at $\lambda = 1.31/1.55$ µm. However, such IR sources of *b*-Si are usually not stable enough for applications. For example, the IR absorption at 1.31/1.55 µm can be significantly reduced by annealing at 775 K for just half an hour.[20]

Recently, Zhao et al. reported another form of *b*-Si, which was fabricated by nanosecond laser pulses without any intentional elemental doping except for using a protective inert gas, like argon (Ar).[24,25] It was quite unexpected that the photodiode based on this *b*-Si has a high and stable photoresponsivity of 260 mA W^{-1} at 5 V and $\lambda = 1.31$ µm,[25] which paves the way for practical sensing by a Si detector at the IR communication wavelength. However, such results are counterintuitive at first glance for the reasons below. Argon is a noble gas widely used as a protective gas in the electronic industry. Due to its fully occupied valence shell with eight electrons, there can be little chemistry between argon and other elements. As a matter of fact, the name of argon, derived from a *Greek* word, means lazy or inactive. Therefore, it is widely expected that Ar should have no effect on the function of semiconductors.

In this study, we report the observation of a very high concentration of Ar (10^{17}-10^{20} cm^{-3}) in ultrafast laser-modified Si using secondary-ion mass spectrometry (SIMS) measurement. First-principles calculations, molecular dynamic simulations, and Hall effect measurement reveal the atomic and electronic structures of Ar-doped Si, which result in unexpectedly strong IR absorption below the bandgap, like at 1.31 µm, and also the effective donor doping. While indeed Ar has negligible effects on the electronic

N.-K. Chen, Y.-C. Gao, J.-H. Zhao, C.-H. Li, Q.-D. Chen, X.-B. Li
State Key Laboratory of Integrated Optoelectronics
College of Electronic Science and Engineering
Jilin University
Changchun 130012, China
E-mail: zhaojihong@jlu.edu.cn; lixianbin@jlu.edu.cn
H.-B. Sun
State Key Lab of Precision Measurement Technology and Instruments
Department of Precision Instrument
Tsinghua University
Beijing 100084, China
E-mail: hbsun@tsinghua.edu.cn
S. Zhang
Department of Physics, Applied Physics, and Astronomy
Rensselaer Polytechnic Institute
Troy, NY 12180, USA
E-mail: zhangs9@rpi.edu
The ORCID identification number(s) for the author(s) of this article can be found under https://doi.org/10.1002/adom.202400361

DOI: 10.1002/adom.202400361

© 2024 Wiley-VCH GmbH

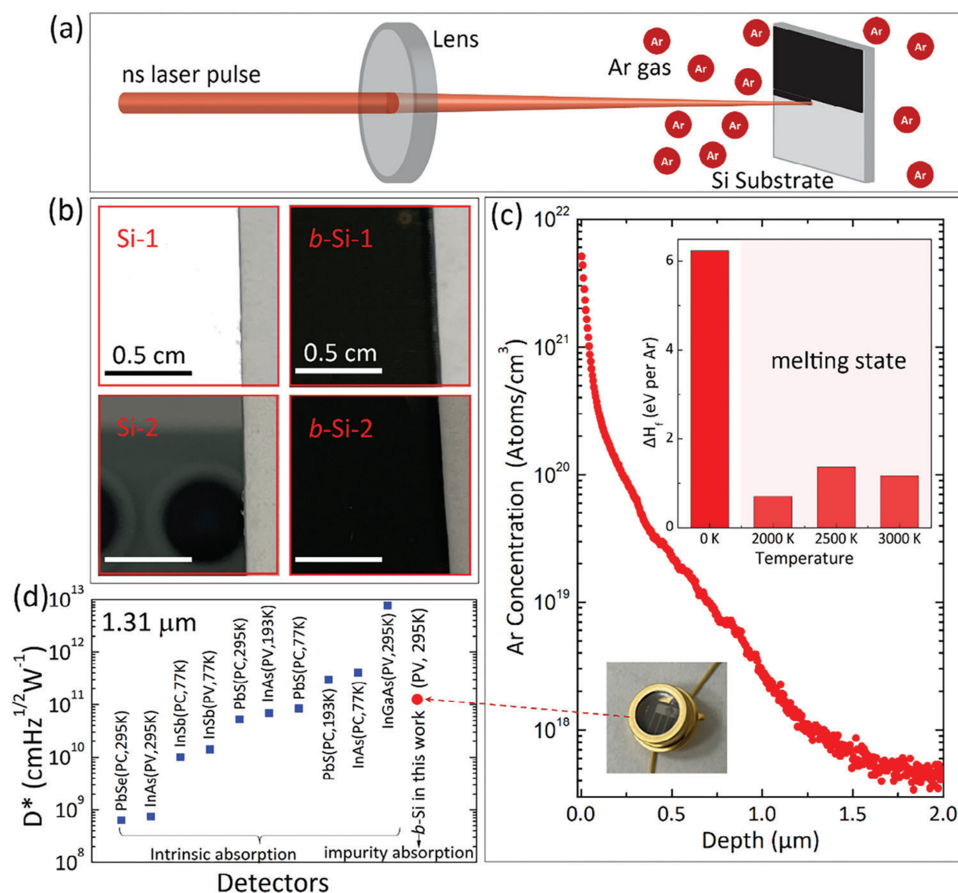

Figure 1. Ar in *b*-Si and its high performance for sub-bandgap IR sensing. a) Schematic of the ns-laser modification of Si in Ar atmosphere. b) Pictures of Si samples before (i.e., unmodified Si) and after (i.e., *b*-Si) laser modification from two camera-shooting angles (1, 2). The scale bar is 0.5 cm. c) Concentration of Ar in ananosecond laser-modified silicon measured by SIMS. Right-upper inset shows the calculated formation energies of *AFV* in crystalline Si at 0 K and in liquid Si at high temperatures. Left-lower inset shows the image of a sub-bandgap IR detector based on the Ar-doped *b*-Si. d) Comparison of specific detectivity (D*) at 1.31 µm between detectors made of *b*-Si and other non-Si materials.[29] Here, PC and PV are for photoconductive and photovoltaic detectors, respectively. The D* of the intrinsic Si detector at 1.31 µm is theoretically 0.

properties of perfect Si, the situation is far different when defects are present. For example, vacancies in Si produce dangling-bond (DB) states within the bandgap, which are unstable as the vacancies can be created, move, cluster, or vanish at elevated temperatures. In contrast, chemically inert Ar can lock a Si vacancy (V_{Si}) to form a stable complex called Ar-filled-vacancy (*AFV*) here, even up to 900 K, whereby locking the DB states of the V_{Si} inside the bandgap. Moreover, the rattling motion of Ar and steric repulsion between its valence electrons and those electrons of the dangling bonds can lead to an enhanced structural distortion that further splits the vacancy levels inside the bandgap and thus induces a strong sub-bandgap IR absorption. Furthermore, the higher-energy partially occupied DB states make the Ar-V_{Si} complex a shallow donor. This explains the puzzle of why laser irradiation results in n-type doping in these samples. Our findings not only propose a critical physics picture to resolve the longtime difficulty of achieving high photoresponsivity of Si-based detectors at the IR communication wavelength but also shed new light on utilizing inert elements to alter the performances of semiconductor devices, which updates current knowledge of defect physics.

2. Results and Discussion

2.1. High Concentration of Ar in Black Si and Its High Specific Detectivity at 1.31 µm

The Si samples were modified by a nanosecond laser under the argon atmosphere (see the schematic of the fabrication process in **Figure 1a**), which has been reported in our previous work (see Methods section).[25] Figure 1b shows the Si samples before and after the laser modification from two camera shooting angles (1, 2), where the clear reflected images of the lamp light (1) and the camera lens (2) can be observed from the surface of the unmodified Si but nothing from the modified *b*-Si, indicating a successful fabrication of *b*-Si. To figure out the role of Ar in the laser-modified Si, we analyzed the dose of Ar by dynamic secondary ion mass spectrometer (SIMS). Figure 1c shows the Ar concentration for a typical *b*-Si sample. Despite that the sample was made more than 1300 days ago, a very high Ar concentration is still detected to be $\approx 5 \times 10^{21}$ cm^{-3} at the surface and $\approx 5 \times 10^{17}$ cm^{-3} at 2 µm below the surface. The results indicate that the Ar atoms have been heavily doped into the Si lattice accompanied by melting and

© 2024 Wiley-VCH GmbH

21951071, 0, Downloaded from https://onlinelibrary.wiley.com/doi/10.1002/adom.202400361 by Jilin University, Wiley Online Library on [09/06/2024]. See the Terms and Conditions (https://onlinelibrary.wiley.com/terms-and-conditions) on Wiley Online Library for rules of use; OA articles are governed by the applicable Creative Commons License

re-solidification process of laser-matter interaction.[26] Moreover, after annealing at 873 K for 30 min in a tube furnace with argon flow, the concentration of Ar atoms is still significant, indicating a good thermal stability of the *b*-Si (see Figure S1, Supporting Information).

Note that the formation energy of Ar doped in crystalline Si at 0 K is high due to its chemical inertness. Table S1 and Figure S2 (Supporting Information) summarize the formation energies (ΔH_f, calculated by density-functional theory) for various defects and their respective atomic configurations, also see Method for more details. For example, for Si vacancy (V_{Si}), $\Delta H_f = 3.69$ eV. When V_{Si} is filled by an Ar atom (i.e., *AFV*), ΔH_f of an *AFV* is as high as $\approx$ 6.3 eV. These results agree with previous calculations.[27,28] However, at elevated temperatures, for example when Si is melted by laser irradiation, the formation energy of *AFV* can be substantially lowered to $\approx$ 1 eV in the liquid Si within the temperature range of 2000 to 3000 K, see the right-upper inset in Figure 1c. Therefore, the ultrafast laser can really introduce Ar into Si, clearly supporting the high concentration of Ar measured by SIMS in the *b*-Si sample.

We evaluate the specific detectivity (D*) of the photodetector based on the *b*-Si sample (left-lower inset of Figure 1c) at IR wavelength $\lambda = 1.31$ µm (see Experimental Section for more details), whose energy is below the Si bandgap and is hence out of the detecting limit of intrinsic Si, and compare the result to those of non-silicon photodetectors based on their intrinsic absorptions.[29] Usually a higher D* corresponds to a higher signal-to-noise ratio for a detector. For example, Figure 1d shows that the D* of the *b*-Si defector can reach 10^{11} cmHz$^{1/2}$W^{-1} even working at 295 K. It is not only higher than those for PbSe and InAs working at the same temperature but also higher than or close to those for InAs and InSb working at much lower temperatures of 193 and 77 K, respectively. Hence, the inclusion of Ar into Si by laser modification potentially offers a highly effective IR absorption avenue for detectors.

2.2. Atomic and Electronic Origin of the Effective Infrared Absorption by Ar

Since Ar has traditionally been regarded as a non-dopant element, it is essential to explore the microscopic roles of Ar in the effective infrared absorption by quantum-precise first-principles calculations. **Figure** 2a–c shows the local atomic structures of bulk Si, V_{Si}, and *AFV*, respectively, all calculated in 216-atom supercells. When a Si atom is removed to form a V_{Si}, four Si DBs are created (see Figure 2b). Here, the four Si atoms closest to the V_{Si} are denoted Si_1, Si_2, Si_3, and Si_4, respectively, and the separations between any pair of them are denoted as $L_{i,j}$. Before the vacancy creation, $L_{i,j} = 3.87$ Å. However, due to the presence of V_{Si}, these Si (with DBs) are relaxed inward to result in $L_{1,2} = 3.03$ Å, $L_{3,4} = 3.12$ Å, while all others are $L_{i,j} = 3.54$ Å. The symmetry is lowered to near D_{2d} from the original T_d. These results agree with previous calculations.[30] Figure 2d–f plots the band structure using the unfolding scheme,[31] namely, unfolding the supercell band structures to that of the primitive cell of intrinsic Si. Based on them, for better observation, Figure 2g–i depicts the schematic positions of defect levels inside the bandgap, which can be grouped into occupied (solid line) and empty (dashed line) states.

AFV, as it occupies a V_{Si} site, significantly modifies the local structure of the V_{Si}. This can be seen by comparing Figure 2c and Figure 2b. Here, Ar pushes the Si atoms with DBs away, so $L_{1,2}$ increases to 3.46 Å whereas $L_{3,4}$ increases to 5.40 Å. The bond angle around Si_3 and Si_4 is increased to $\approx$120°, indicating that the local hybridization type for these Si atoms has changed from sp^3 to sp^2. In contrast, Si_1 and Si_2 maintain the usual sp^3 hybridization type. As a result, the symmetry is further lowered from near D_{2d} for V_{Si} to C_{2v} for an *AFV*. These structural changes cost energy, as taking an *Ar* atom from the vacuum and placing it at a V_{Si} requires an extra energy of 2.56 eV. The reason for the energy increase is the repulsive interaction between electrons in the closed shell of *Ar* and those of the DBs of V_{Si}. Because Ar is chemically inert, there is neither a charge transfer nor shared electrons with its neighboring Si atoms with DBs (Figure S3, Supporting Information). This, coupled with the symmetry reduction, results in a significant splitting of the DB states of V_{Si}, as the new defect states for *AFV*. In particular, the two occupied states are split by almost 1 eV, pushing the (red) $Si_{1,2}$ state up while pushing the (green) $Si_{3,4}$ state down. Due to orthogonality between wavefunctions, the pushed-up $Si_{1,2}$ state in turn pushes up the two empty DB states, as can be seen by comparing Figure 2h with Figure 2i. Importantly, the gaps between the occupied and empty defect states are significantly reduced relative to V_{Si}, which explains why *AFV* is a good candidate for IR absorption. For localized defect states, one needs to consider the effect of spin (Figure S4 and S5, Supporting Information), which has been taken care of in our discussion.

Note that the C_{2v} symmetry is not unique to *AFV*. For example, *AFV* can also assume approximate C_{3v} or T_d symmetry, respectively, see Figure S2b,c (Supporting Information). In both cases, the Si atoms with DBs are pushed away, leading to the sp^2-like hybridization. Thus, all *AFV* defects exhibit some sort of steric-repulsive distortion (SRD) and they also have almost identical formation energies with differences just within 0.01-0.03 eV (Table S1, Supporting Information). The energy barrier for transition between the C_{2v} and C_{3v} configurations and that between C_{3v} and T_d configurations, calculated by the c-NEB method, are 0.015 and 0.013 eV, respectively. These small barriers suggest that transitions between different *AFV* structures will take place rapidly at room temperature inside the vacancy (Figure S6, Supporting Information). On the other hand, regardless of the local structure, their defect levels are always inside the bandgap (Figures S4 and S5, Supporting Information). SRD also exists in clusters that are made of multiple *AFV*s (e.g., $(AFV)_2$, $(AFV)_3$, and $(AFV)_4$ in Figure S2, Supporting Information) with appreciable splitting of defect levels (Figure S7, Supporting Information).

To demonstrate the role of these defect states in optical absorption, we apply the meta-GGA approach with the modified Becke-Johnson (MBJ) exchange potential.[32,33] The approach yields the correct Si bandgap (Figure S8, Supporting Information), which is usually underestimated by PBE. Figure 2j shows the optical absorption coefficient for *AFV* with SRD. A significant enhancement of sub-bandgap IR absorption is indeed found in all *AFV* defects regardless of their local atomic structure, in great contrast to the very weak IR absorption of intrinsic Si. In fact, the *AFV*s also have stronger absorptions than V_{Si}. The large absorptance of

© 2024 Wiley-VCH GmbH

21951071, 0, Downloaded from https://onlinelibrary.wiley.com/doi/10.1002/adom.202400361 by Jilin University, Wiley Online Library on [09/06/2024]. See the Terms and Conditions (https://onlinelibrary.wiley.com/terms-and-conditions) on Wiley Online Library for rules of use; OA articles are governed by the applicable Creative Commons License

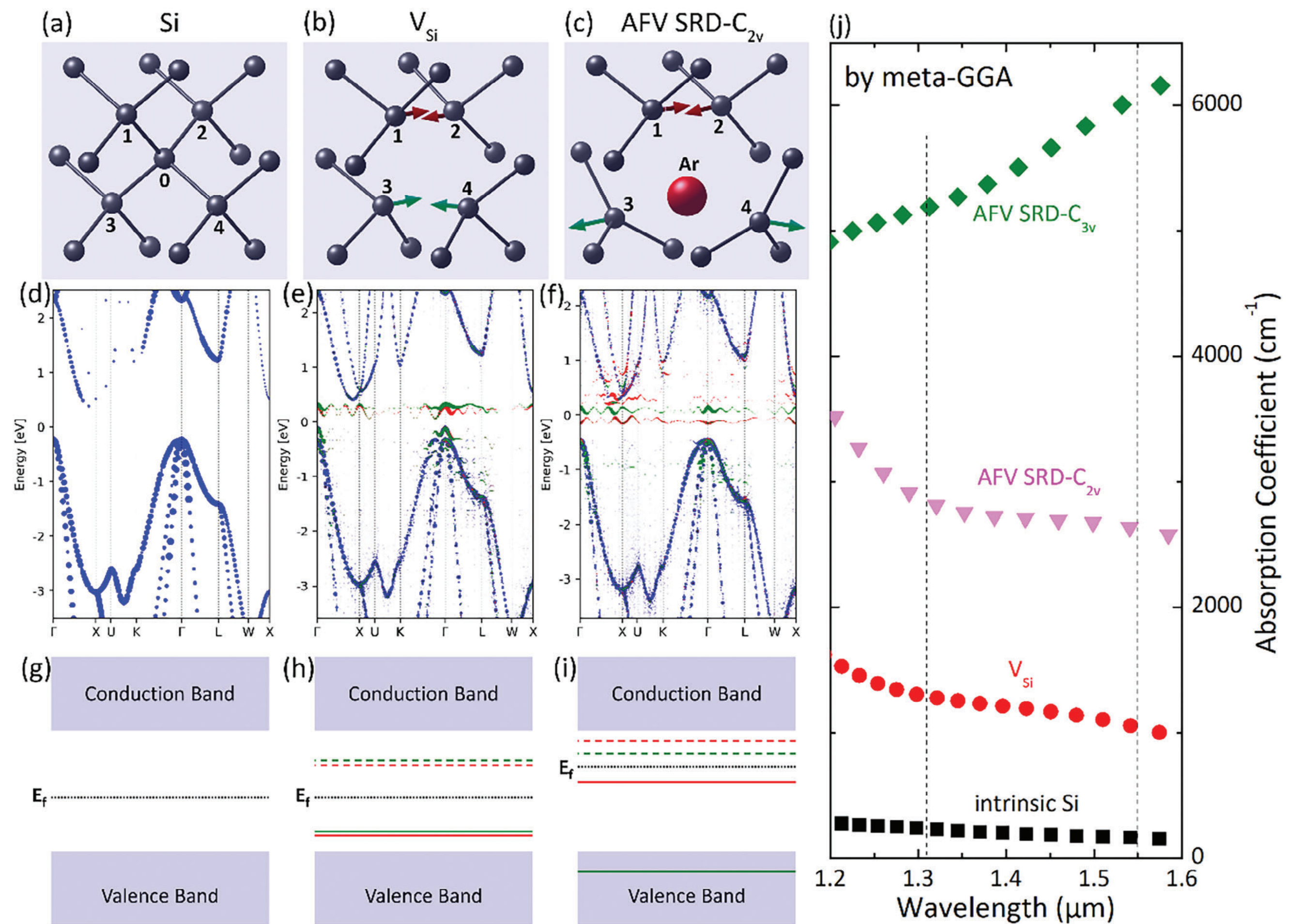

Figure 2. Modulation of local atomic structure and electronic structure of silicon by V_{Si} and *AFV* defects. Local structure of a) intrinsic Si, b) V_{Si}, and c) *AFV* with a C_{2v} symmetry due to steric-repulsive distortion (SRD). Arrows indicate directions of atomic relaxations compared to their ideal lattice position. d–f) The corresponding unfolded band structures. The size of the scatters indicates atomic weight. The four Si atoms marked in panels (a-c) form two groups: $Si_{1,2}$ and $Si_{3,4}$, whose scatters are colored red and green, respectively, and are enlarged by a factor of 10. E_f is set at 0 eV. Panels (g-i) show schematically the corresponding defect levels inside the bandgap (solid line for occupied states, dashed line for empty states). The meaning of red/green color is the same as that in (d-f). j) Calculated optical absorption coefficient for intrinsic *Si*, V_{Si}, and *AFVs* with C_{2v} and C_{3v} SRD.

the *b*-Si sample is also confirmed by experimental measurements (Figure S9, Supporting Information).

2.3. Origin of the Abnormal n-Type Doping Effect by Ar

Figure 3a shows the measured sheet carrier concentration (N_s) of the fabricated *b*-Si compared to that of the unmodified Si substrate. Obviously, the carrier concentrations of the *b*-Si are greatly enhanced. For example, the N_s of a *b*-Si sample (2.3×10^{13} cm^{-2}) at 300 K is two orders of magnitude higher than that before the laser modification (3.3×10^{10} cm^{-2}). Moreover, the measured Hall coefficients (R_{HS}) in Figure 3b are all negative from 200 to 400 K. These strongly indicate the *b*-Si samples are n^+-type or strong electron conductive. This result seems counterintuitive because Ar itself cannot act as an ionized impurity due to its inertia. Therefore, we further analyze the doping property of the *AFVs* by first-principles calculations of ionization energy (E_I). The results in Figure 3c demonstrate that the *AFV* indeed holds a lower donor E_I than its acceptor E_I while the V_{Si} shows the opposite. In fact, the donor E_I of *AFVs* can be as low as 0.074 – 0.112 eV, indicating its good tendency to offer electrons to the conduction band. The result can be understood from a phenomenological point of view: Ar valence electrons are in a close shell with noticeably lower energies than those of Si. Due to steric repulsion, therefore, the high-lying V_{Si} states are pushed up in energy by the Ar. Note that some of the V_{Si} states are occupied. Repulsion by Ar makes their ionization into the conduction band edge much easier. This is consistent with the experimental fact in Figure 3a,b that the *b*-Si with Ar exhibit substantially increased *n*-type carrier concentration.

2.4. Dynamic Stability of Ar-Filled Vacancy Versus Pure Vacancy in Si

While our results for *AFV* agree well with experimental observations, we note that the V_{Si}, which has the lower ΔH_f (of 3.69 eV),

© 2024 Wiley-VCH GmbH

21951071, 0, Downloaded from https://onlinelibrary.wiley.com/doi/10.1002/adom.202400361 by Jilin University, Wiley Online Library on [09/06/2024]. See the Terms and Conditions (https://onlinelibrary.wiley.com/terms-and-conditions) on Wiley Online Library for rules of use; OA articles are governed by the applicable Creative Commons License

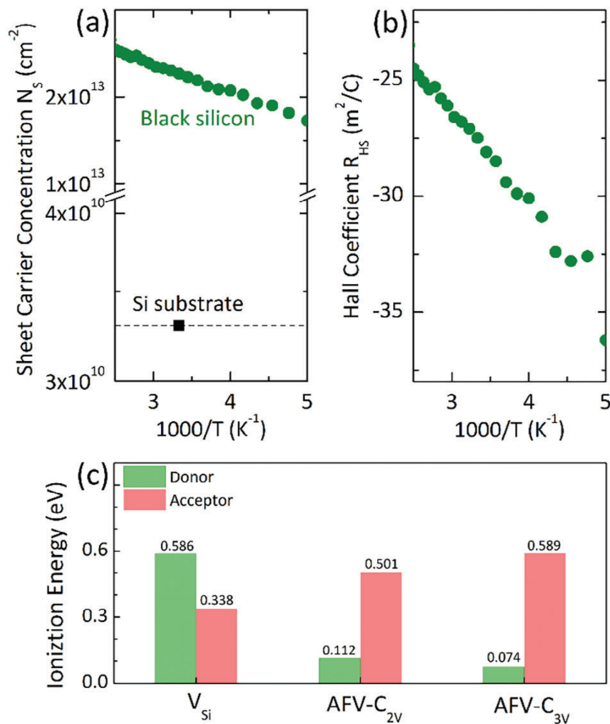

Figure 3. Abnormal n-type doping in *b*-Si by Ar. a) Sheet carrier concentration (N_s) of *b*-Si at different temperatures. b) Temperature-dependent Hall coefficient (R_{HS}) of the *b*-Si. c) Defect ionization energy (E_I) of V_{Si}, *AFV* with C_{2v} SRD, and *AFV* with C_{3v} SRD. The ionization energies of the donor and acceptor are determined by calculating transition levels with respect to CBM and VBM, respectively.[34,35] E_I for *AFV*-C_{2v} are determined by transition level of $\varepsilon(+1/-1)$ while other values are determined by $\varepsilon(+1/0)$ or $\varepsilon(0/-1)$.

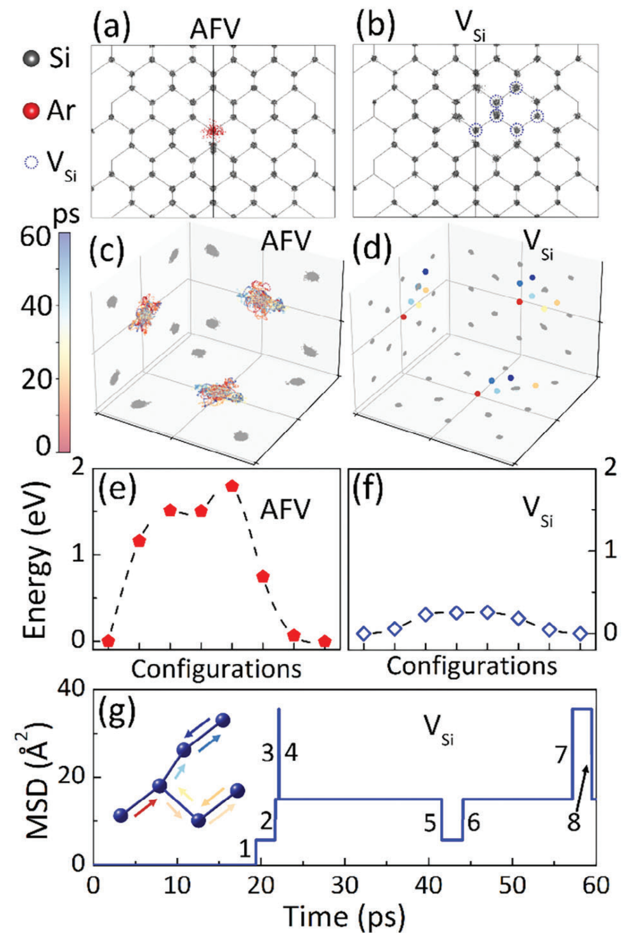

Figure 4. Stability and Migration Barrier of *AFV* and V_{Si} defects in silicon. The atomic trajectory for a) *AFV* and (b) V_{Si} during 60-ps MDs at 500 K, viewed on a Si (1$\bar{1}$0) cross-section. Blue circles in (b) denote the positions of V_{Si} during the MD. c) and d) show the projected trajectories corresponding to **a** and **b**, respectively. e) and f) show the corresponding migration barriers calculated by the c-NEB method. g) MSD for V_{Si} during the MD. Inset in (g) shows the schematical trajectory where arrows indicate the movement route of V_{Si}.

contains gap states and would also result in sub-bandgap IR absorption. To understand why Ar is needed in the experiment, we consider the dynamic stability of V_{Si} and *AFV* by performing ab initio molecular dynamics (MD) simulations at 500 K. However, to study the dynamics of a vacancy, one issue is how to define its position. Here, we use the Wigner-Seitz method, as implemented in the OVITO code.[36] **Figure** 4a–d shows the atomic trajectories over a time period of 60 ps. We see that *AFV* moves around its central position, much more rapidly than a Si atom on the lattice, which is consistent with the fact that the energy barriers between different *AFV*-SRD configurations are negligibly small. Despite the rapid local motion, *AFV* stays inside the same vacancy during the entire simulation without a long-range diffusion. In contrast, V_{Si} diffuses rapidly between lattice sites. Hence, it is not locked at any given lattice site. Figure 4g shows the mean square displacement (MSD) for V_{Si}, revealing as many as 8 hops between sites within 60 ps. These results suggest that the diffusion barriers for *AFV* and V_{Si} are drastically different.

To confirm, we perform calculations using the c-NEB method. It is found that the barrier (E_a) for an *AFV* migration to its nearby lattice is as high as 1.8 eV (Figure 4e). To be certain, we have also considered several other diffusion paths of *AFV*s but the results are nearly the same, see Figure S10 (Supporting Information) for details. Using the Arrhenius equation: $P = \nu \exp(-\frac{E_a}{k_B T})$, where k_B is the Boltzmann constant, $T = 500$ K is the temperature, and $\nu \approx 15$ THz is the attempt frequency,[37] we obtain the migration time to be $\tau = 1/P \approx 26$ hours. Even for $T = 900$ K (the annealing temperature used in fabricating the black Si detectors),[25] we obtain $\tau \approx 1$ ms for one lattice hop. Not surprisingly, a 60-ps MD at 900 K (**Figure** 5a–c) also did not yield any migration of *AFV*. In contrast, the barrier for V_{Si} diffusion can be as low as $E_a = 0.26$ eV (Figure 4f). The corresponding migration time at $T = 500$ K is as short as $\tau \approx 28$ ps, which is indeed on the same order of magnitude as the MD simulation has. Hence, although V_{Si} is an IR source, it is not a stable one, as it can readily migrate to grain boundaries or out of samples upon annealing at elevated temperatures.

Next, we further test the stabilities for a multi-defect condition of *AFV*s. First, Figure 5d displays the trajectory of four clustering *AFV*s [$(AFV)_4$] at 500 K. The projected trajectories onto planes (100), (010), and (001) are also shown in Figure 5e. It is clearly demonstrated that even though four Ar fill in four nearby vacancies in the form of the *AFV* cluster, they still have robust

 © 2024 Wiley-VCH GmbH

21951071, 0, Downloaded from https://onlinelibrary.wiley.com/doi/10.1002/adom.202400361 by Jilin University, Wiley Online Library on [09/06/2024]. See the Terms and Conditions (https://onlinelibrary.wiley.com/terms-and-conditions) on Wiley Online Library for rules of use; OA articles are governed by the applicable Creative Commons License

21951071, 0, Downloaded from https://onlinelibrary.wiley.com/doi/10.1002/adom.202400361 by Jilin University, Wiley Online Library on [09/06/2024]. See the Terms and Conditions (https://onlinelibrary.wiley.com/terms-and-conditions) on Wiley Online Library for rules of use; OA articles are governed by the applicable Creative Commons License

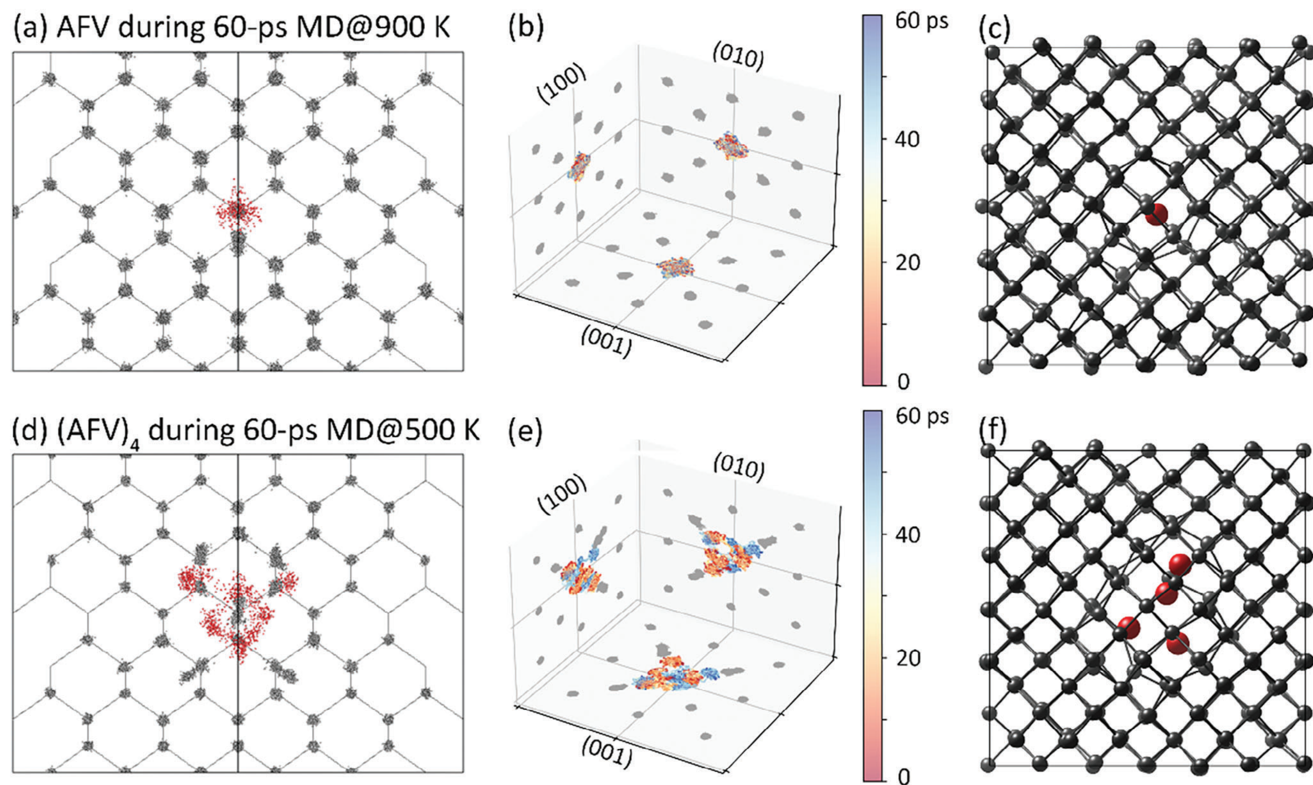

Figure 5. Dynamic stability of *AFV* at high-temperature and multi-defect conditions. a) Atomic trajectory during a 60-ps MD at 900 K, viewed on the $(1\bar{1}0)$ cross-section. The time step of the trajectory is 0.2 ps. b) The projected trajectory onto different planes corresponding to **a**. c) A transient structure of *AFV* at the last stage of the high-temperature MD. d–f) The atomic trajectory, the projected trajectory, and the transient structure of four clustering *AFV*s, that is, $(AFV)_4$ during the 60-ps MD at 500 K.

stability without any long-range diffusion, which is also supported by their last local structure in Figure 5f.

The physical picture above reveals the important benefits of using "*inert*" Ar as in fact the "*active*" dopant for IR detectors at the forbidden wavelength of intrinsic Si. First, the band splitting broadens the absorption spectrum to a point even better than that of the V_{Si}. Second, besides the static effect, the existence of multiple Ar configurations on the same site with very similar energies and exceptionally low barriers (Figures S2,S4, and S5 in Supporting Information) enables a dynamic broadening of the spectrum especially at elevated temperatures. These enhancements are due to both steric and dynamic repulsions by Ar orbitals to Si dangling bonds in *AFV*s. Third, Ar can act as an unexpected electronic impurity with relatively shallow donor levels. As a result, an n^+ layer can be readily fabricated on the n^--Si substrate, which is very important for the construction of n^+-n^- junction to achieve *b*-Si IR detectors at the originally forbidden wavelength of intrinsic Si, like 1.31 or 1.55 µm.[25] Finally, the robust dynamic stability of *AFV*s guarantees the stable performance of *b*-Si devices.

3. Conclusion

In summary, we detect an exceptionally high level of Ar (10^{17}–10^{20} cm^{-3}) in laser-modified *b*-Si samples by the SIMS measurement, even though these samples were fabricated more than 1300 days ago under the protective Ar atmosphere. First-principles calculation, molecular dynamics simulations, and Hall effect measurements together reveal the unexpected roles of Ar. While a V_{Si} readily migrates at 500 K, *AFV* is locked in space at even a higher temperature, in spite that there is no chemical bond between Ar and neighboring Si atoms. Ar also modifies the electronic structure of V_{Si}, leading to a significant broadening of the sub-bandgap energy levels. Moreover, the steric repulsion between Ar and DB electronic states gives rise to a shallow donor behavior, which explains the puzzling *n*-typeness of laser-irradiated samples. It is reasonable to expect that the microscopic picture of inert element-induced IR absorption discovered here in Si may also happen in other semiconductors. Therefore, our work points to a new direction of using inert elements for applications in advanced electronics. What's more, the defect physics in semiconductors will be also updated.

4. Experimental Section

First-Principles Calculation and Molecular Dynamics: Density-functional theory (DFT) calculations were performed using the VASP code,[38,39] in which the projector-augmented wave (PAW) pseudo potential[40,41] and generalized-gradient approximation (GGA) exchange-correlation functional developed by Perdew, Burke, and Ernzerh were adopted.[42] A 216-Si atom supercell was used to mimic the defect complexes. The energy cut-off for the plane-wave expansion was 380 eV. For Brillouin-zone sampling, Γ point was used for structural relaxation and molecular dynamic (MD)

© 2024 Wiley-VCH GmbH

21951071, 0, Downloaded from https://onlinelibrary.wiley.com/doi/10.1002/adom.202400361 by Jilin University, Wiley Online Library on [09/06/2024]. See the Terms and Conditions (https://onlinelibrary.wiley.com/terms-and-conditions) on Wiley Online Library for rules of use; OA articles are governed by the applicable Creative Commons License

simulation, while a 3×3×3 Monkhorst-Pack k-point grid was used in the total energy and electronic structure calculations. The MD simulations use the *NVT* ensemble with a time step of 2 fs. Band structures of the supercells were unfolded using the modified *VaspBandUnfolding* package.[43] Energy barriers were calculated using the climbing image nudged elastic band (c-NEB) method.[44,45] Visualizations of the atomic structure and charge density were done using the VESTA code.[46] Positions of the V_{Si} were determined by the Wigner-Seitz method in the OVITO code.[36] The energies of *AFV*s in liquid Si (to evaluate the formation energy) were obtained by performing 20-ps *NVT* MD simulations, extracting free energies between 10 and 20 ps (totally 5000 frames), and then taking their average. More calculation details of formation energy and absorption coefficient are presented in Notes S1 and S2 (Supporting Information).

Fabrication and Characterization: The fabrication details of *b*-Si samples by ns-laser were reported in our previous work.[25] The *b*-Si was fabricated with a laser power of 20 mW and a laser fluence of 7.88 J cm^{-2}. The concentration of Ar in laser-modified *b*-Si samples was measured by a dynamic secondary ion mass spectrometer (D-SIMS). The D-SIMS instrument was equipped with a Cameca IMS-4F device using the 8 keV Cs^+ primary beam. The electrical characteristics including sheet carrier concentration N_s and temperature dependent Hall coefficient R_{HS} of *b*-Si samples were obtained by an ACCENT HL5500PC Hall system based on the Van der Pauw method. More details of the fabrication, the absorptance, the responsivity, and specific detectivity are presented in Notes S3 and S4 (Supporting Information).

Supporting Information

Supporting Information is available from the Wiley Online Library or from the author.

Acknowledgements

N.C. and Y.G. contributed equally to this work. Work in China was supported by the National Science and Technology Major Project (Grant No. 2022ZD0117600), the National Natural Science Foundation of China (Grants No. 62275098, No. 12274180, No. 12274172), the Natural Science Foundation of Jilin Province (No. 20230101007JC) and the Fundamental Research Funds for the Central Universities. S.Z. was supported by the US Department of Energy under Award No. DE-SC0002623. The authors sincerely thank Prof. Q.Z. at USTC for his support of band-unfolding analysis. The High-Performance Computing Center (HPCC) at Jilin University for computational resources is also acknowledged.

Conflict of Interest

The authors declare no conflict of interest.

Data Availability Statement

The data that support the findings of this study are available from the corresponding author upon reasonable request.

Keywords

defect physics, first-principles calculations, infrared detector, silicon-based optoelectronics

Received: February 6, 2024
Revised: May 6, 2024
Published online:

[1] M. Delaney, I. Zeimpekis, H. Du, X. Yan, M. Banakar, D. J. Thomson, D. W. Hewak, O. L. Muskens, *Sci. Adv.* **2021**, *7*, eabg3500.
[2] A. Durand, Y. Baron, W. Redjem, T. Herzig, A. Benali, S. Pezzagna, J. Meijer, A. Y. Kuznetsov, J. M. Gérard, I. Robert-Philip, M. Abbarchi, V. Jacques, G. Cassabois, A. Dréau, *Phys. Rev. Lett.* **2021**, *126*, 083602.
[3] D. Guo, P. Guo, L. Ren, Y. Yao, W. Wang, M. Jia, Y. Wang, L. Wang, Z. L. Wang, J. Zhai, *Sci. Adv.* **2023**, *9*, eadd3310.
[4] C. Han, Z. Zheng, H. Shu, M. Jin, J. Qin, R. Chen, Y. Tao, B. Shen, B. Bai, F. Yang, Y. Wang, H. Wang, F. Wang, Z. Zhang, S. Yu, C. Peng, X. Wang, *Sci. Adv.* **2023**, *9*, eadi5339.
[5] D. B. Higginbottom, A. T. K. Kurkjian, C. Chartrand, M. Kazemi, N. A. Brunelle, E. R. MacQuarrie, J. R. Klein, N. R. Lee-Hone, J. Stacho, M. Ruether, C. Bowness, L. Bergeron, A. DeAbreu, S. R. Harrigan, J. Kanaganayagam, D. W. Marsden, T. S. Richards, L. A. Stott, S. Roorda, K. J. Morse, M. L. W. Thewalt, S. Simmons, *Nature* **2022**, *607*, 266.
[6] C. Rogers, A. Y. Piggott, D. J. Thomson, R. F. Wiser, I. E. Opris, S. A. Fortune, A. J. Compston, A. Gondarenko, F. Meng, X. Chen, G. T. Reed, R. Nicolaescu, *Nature* **2021**, *590*, 256.
[7] G. Zheng, N. Samkharadze, M. L. Noordam, N. Kalhor, D. Brousse, A. Sammak, G. Scappucci, L. M. K. Vandersypen, *Nat. Nanotechnol.* **2019**, *14*, 742.
[8] S. Li, X. Liu, H. Yang, H. Zhu, X. Fang, *Nat. Electron.* **2024**, *7*, 216.
[9] W. Yang, J. Chen, Y. Zhang, Y. Zhang, J. H. He, X. Fang, *Adv. Funct. Mater.* **2019**, *29*, 1808182.
[10] N. Flöry, P. Ma, Y. Salamin, A. Emboras, T. Taniguchi, K. Watanabe, J. Leuthold, L. Novotny, *Nat. Nanotechnol.* **2020**, *15*, 118.
[11] X. Wang, X. Zhuang, S. Yang, Y. Chen, Q. Zhang, X. Zhu, H. Zhou, P. Guo, J. Liang, Y. Huang, A. Pan, X. Duan, *Phys. Rev. Lett.* **2015**, *115*, 027403.
[12] S. Mauthe, Y. Baumgartner, M. Sousa, Q. Ding, M. D. Rossell, A. Schenk, L. Czornomaz, K. E. Moselund, *Nat. Commun.* **2020**, *11*, 4565.
[13] P. Piquini, P. A. Graf, A. Zunger, *Phys. Rev. Lett.* **2008**, *100*, 186403.
[14] J. H. Vella, L. Huang, N. Eedugurala, K. S. Mayer, T. N. Ng, J. D. Azoulay, *Sci. Adv.* **2021**, *7*, eabg2418.
[15] P. Wen, P. Tiwari, S. Mauthe, H. Schmid, M. Sousa, M. Scherrer, M. Baumann, B. I. Bitachon, J. Leuthold, B. Gotsmann, K. E. Moselund, *Nat. Commun.* **2022**, *13*, 909.
[16] A. Rogalski, *Infrared Phys. Techn.* **2002**, *43*, 187.
[17] A. Pelella, A. Grillo, E. Faella, G. Luongo, M. B. Askari, A. Di Bartolomeo, *ACS Appl. Mater. Interfaces* **2021**, *13*, 47895.
[18] J. E. Carey, C. H. Crouch, M. Shen, E. Mazur, *Opt. Lett.* **2005**, *30*, 1773.
[19] M. Tabbal, T. Kim, D. N. Woolf, B. Shin, M. J. Aziz, *Appl. Phys. A* **2009**, *98*, 589.
[20] B. R. Tull, M. T. Winkler, E. Mazur, *Appl. Phys. A* **2009**, *96*, 327.
[21] T. Baldacchini, J. E. Carey, M. Zhou, E. Mazur, *Langmuir* **2006**, *22*, 4917.
[22] C.-H. Li, J.-H. Zhao, X.-Y. Yu, Q.-D. Chen, J. Feng, P.-D. Han, H.-B. Sun, *IEEE Sens. J.* **2017**, *17*, 2367.
[23] M. T. Winkler, D. Recht, M.-J. Sher, A. J. Said, E. Mazur, M. J. Aziz, *Phys. Rev. Lett.* **2011**, *106*, 178701.
[24] C. H. Li, J. H. Zhao, Q. D. Chen, J. Feng, H. B. Sun, *Opt. Lett.* **2018**, *43*, 1710.
[25] J.-H. Zhao, C.-H. Li, X.-B. Li, Q.-D. Chen, Z.-G. Chen, H.-B. Sun, *IEEE T. Electron. Dev.* **2018**, *65*, 4905.
[26] M.-J. Sher, M. T. Winkler, E. Mazur, *MRS Bull.* **2011**, *36*, 439.
[27] F. Corsetti, A. A. Mostofi, *Phys. Rev. B* **2011**, *84*, 035209.
[28] L. Pizzagalli, A. Charaf-Eddin, S. Brochard, *Comput. Mater. Sci.* **2014**, *95*, 149.
[29] A. Rogalski, presented at *Proc. SPIE 10433, Electro-Optical and Infrared Systems: Technology and Applications XIV*, Warsaw, POLAND, 104330L, October, **2017**.
[30] M. J. Puska, S. Pöykkö, M. Pesola, R. M. Nieminen, *Phys. Rev. B* **1998**, *58*, 1318.

 © 2024 Wiley-VCH GmbH

[31] V. Popescu, A. Zunger, *Phys. Rev. B* **2012**, *85*, 085201.
[32] A. D. Becke, E. R. Johnson, *J. Chem. Phys.* **2006**, *124*, 221101.
[33] F. Tran, P. Blaha, *Phys. Rev. Lett.* **2009**, *102*, 226401.
[34] D. Wang, D. Han, X.-B. Li, S.-Y. Xie, N.-K. Chen, W. Q. Tian, D. West, H.-B. Sun, S. B. Zhang, *Phys. Rev. Lett.* **2015**, *114*, 196801.
[35] S. B. Zhang, J. E. Northrup, *Phys. Rev. Lett.* **1991**, *67*, 2339.
[36] A. Stukowski, *Modelling Simul. Mater. Sci. Eng.* **2010**, *18*, 015012.
[37] B. L. Davis, M. I. Hussein, *AIP Adv.* **2011**, *1*, 041701.
[38] G. Kresse, J. Furthmuller, *Comput. Mater. Sci.* **1996**, *6*, 15.
[39] G. Kresse, J. Furthmuller, *Phys. Rev. B* **1996**, *54*, 11169.
[40] P. E. Blochl, *Phys. Rev. B* **1994**, *50*, 17953.
[41] G. Kresse, D. Joubert, *Phys. Rev. B* **1999**, *59*, 1758.
[42] J. P. Perdew, K. Burke, M. Ernzerhof, *Phys. Rev. Lett.* **1996**, *77*, 3865.
[43] https://github.com/QijingZheng/VaspBandUnfolding (accessed: November 2022).
[44] S. A. Trygubenko, D. J. Wales, *J. Chem. Phys.* **2004**, *120*, 2082.
[45] N. A. Zarkevich, D. D. Johnson, *J. Chem. Phys.* **2015**, *142*, 024106.
[46] K. Momma, F. Izumi, *J. Appl. Cryst.* **2011**, *44*, 1272.

© 2024 Wiley-VCH GmbH

21951071, 0, Downloaded from https://onlinelibrary.wiley.com/doi/10.1002/adom.202400361 by Jilin University, Wiley Online Library on [09/06/2024]. See the Terms and Conditions (https://onlinelibrary.wiley.com/terms-and-conditions) on Wiley Online Library for rules of use; OA articles are governed by the applicable Creative Commons License